PAPER

Check for updates

Efficient inactivation of *Microcystis aeruginosa* by carbon microtube-supported magnetic photocatalysts under visible light

Wenli Qin, [ID] †[ab] Xinyi Zhang,†[abc] Gaofeng Chen,[a] Zhaoting Ji[a] and Zengling Ma*[ab]

The increasing influx of nutrients (*e.g.*, nitrogen and phosphorus) into freshwater systems is exacerbating eutrophication in natural waterways. To address this issue, a novel magnetic photocatalyst composed of a carbon nanotube core and a titanium dioxide coating (denoted as $C-TiO_2-Fe_3O_4$ and $C-TiFe_2O_4$) is successfully synthesized. *Microcystis aeruginosa* and microcystin-LR (MC-LR) in eutrophicated water can be efficiently inactivated by the composite *via* visible light photocatalysis. The incorporation of magnetic Fe significantly enhances cyanobacteria capture and improves the photocatalytic efficiency for algal inactivation and MC-LR breakdown. $C-TiFe_2O_4$ exhibits the highest adsorption-photocatalysis performance with an inactivation efficiency of 77.9% after 7 hours. Under optimal conditions (7 h of reaction time, a catalyst dosage of 0.39 g L^{-1}, and an initial algae density of 1×10^6 cells per mL), the MC-LR removal rate is 89.1%. Notably, $C-TiFe_2O_4$ maintains exceptional stability and reusability even after five cycles. The composite demonstrates promising potential for treating harmful algal blooms (HABs) across diverse environmental conditions. These findings highlight the viability of $C-TiFe_2O_4$ as a sustainable and scalable technology to mitigate HABs and degrade MC-LR in contaminated water systems.

Introduction

The rapid expansion of industrial and agricultural activities and the intensifying global greenhouse effect have increased surface water temperatures and nutrient loads in aquatic environments, which have made harmful algal blooms (HABs) caused by cyanobacteria increasingly frequent.[1,2] These blooms monopolize nutrients, release biotoxins, and disrupt aquatic ecosystems by outcompeting other plankton species and degrading their habitats.[3] In addition, these toxins tend to accumulate progressively in marine organisms, such as shellfish and fish, which ultimately threatens human health through food chain contamination.[4] Therefore, it is imperative to develop an efficient and eco-friendly algae removal technology.

Conventional algae removal technologies such as mechanical harvesting, ultrasonic treatment, chemical addition, and biological control often suffer from slow response times, elevated operational expenses, risks of secondary pollution, and other limitations.[5–8]

Advanced oxidation processes (AOPs) have attracted increasing attention because they can generate reactive oxygen species (ROS), which effectively attack and inactivate algal cells in aquatic environments.[9] For example, the photocatalytic technology has low energy demands, high efficiency, and environmental sustainability, making it distinctly more advantageous than alternatives such as electrocatalysis.[10] This approach removes algal cells and partially degrades released organic matter and toxins, making it promising for mitigating harmful algal blooms (HABs).[11] Wei *et al.*[12] synthesized an F–TiO$_2$ nanohybrid that could remove 97.5% of *Microcystis aeruginosa* within 8 h *via* photocatalytic processes. Similarly, Sun *et al.*[13] developed a ternary photocatalyst (g-C$_3$N$_4$@-Bi$_2$MoO$_6$@AgI) that could remove nearly 100% of cyanobacteria after 6 h of visible-light irradiation. Therefore, visible-light-driven photocatalysis has emerged as a highly efficient and sustainable solution to control cyanobacterial blooms.

The selection of appropriate semiconductor materials is crucial to achieve efficient visible light catalysis. The traditional TiO$_2$ powder is not suitable for water treatment because additional recycling operations are required to remove the catalyst after the photocatalytic treatment.[14] To address this challenge, magnetic separation has emerged as one of the most effective methods to retrieve TiO$_2$ nanoparticles from aqueous environments.[15] In addition, the relatively narrow band gap of the magnetic material can extend the light absorption of composite catalysts into the visible spectrum. Therefore, magnetically separated photocatalysts with high stability and good

[a]*National and Local Joint Engineering Research Center of Ecological Treatment Technology for Urban Water Pollution, College of Life and Environmental Science, Wenzhou University, Wenzhou, 325035, P.R. China. E-mail: mazengling@wzu.edu.cn*

[b]*Zhejiang Provincial Key Laboratory of Water Ecological Environment Treatment and Resource Protection, Wenzhou University, Wenzhou, 325035, China*

[c]*College of Optoelectronic Manufacturing, Zhejiang Industry and Trade Vocational College, Wenzhou, 325002, P.R. China*

† These authors contributed equally to this work and should be considered co-first authors.

photocatalytic performance have attracted increasing attention. Among magnetic materials, Fe_3O_4 is the most extensively utilized to date. Zheng et al.[16] prepared Fe_3O_4–C–TiO_2 magnetic nanocomposites using the sol–gel method and demonstrated that Fe_3O_4 incorporation increased visible-light photocatalytic efficiency and enabled facile magnetic recovery from the solution. Yu et al.[17] synthesized a new type of TiO_2–Fe_3O_4 hierarchical porous composite and showed that efficient Fe^{2+} reduction by TiO_2 significantly promoted interfacial charge transfer between components. Therefore, magnetic Fe^{2+} incorporation can simultaneously boost the photocatalytic activity and recyclability of TiO_2-based systems.

In this work, carbon microtube-supported TiO_2 magnetic photocatalysts (C–TiO_2–Fe_3O_4 and C–$TiFe_2O_4$) were prepared, and their properties were evaluated with a focus on enhancing the visible-light photocatalytic performance. Then, the composites were applied to remove *Microcystis aeruginosa*, for which key reaction parameters were optimized, including the composite ratio, catalyst dosage, pH, natural organic matter (NOM) concentration, and initial algal density. The kinetics and mechanisms of photocatalytic algal inactivation were thoroughly investigated. We also examined the physiological changes in algal cells during photocatalysis and elucidated the role of reactive oxygen species (ROS) in the algae removal process. These findings provide valuable mechanistic insights and demonstrate the potential of photocatalysis as an effective strategy for cyanobacterial bloom control.

Experimental

Materials

A corncob powder (<300 mesh) was obtained from Lianyungang Surui Straw Processing Plant Co., Ltd (China). Nitric acid (HNO_3) was obtained from Shanghai Sinopharm Group Chemical Reagent Co., Ltd (China). Tetrabutyl titanate, methanol, ethanol, acetonitrile, acetic acid, trifluoroacetic acid, isopropanol (IPA), hydroquinone (BQ), sodium oxalate (SO), silicon dioxide (SiO_2), humic acid (HA), fulvic acid (FA), sodium hydroxide (NaOH), hydrochloric acid (HCl), $FeCl_3 \cdot 6H_2O$, and $FeSO_4$ were obtained from Shanghai Aladdin Biochemical Technology Co., Ltd (China). MC-LR was purchased from Shanghai Yuanye Biotechnology Co., Ltd (China).

Preparation of magnetic photocatalysts

The carbon microtube-supported photocatalysts (C–TiO_2 and C–TiO_2–Fe_3O_4) were prepared according to the method reported in our previous work.[18] First, 30 mL of ethanol was added to 0.01 mol tetrabutyl titanate and 0.02 mol $FeCl_3 \cdot 6H_2O$. Then, 3 g of the CMT and 20 mL of NaOH (6 mM) were added, stirred for 0.5 h, and heated at 80 °C for 1 h. The particles were filtered, collected, dried completely in an oven at 100 °C, and calcined in a muffle furnace at 900 °C for 3 h to obtain C–$TiFe_2O_4$.

Culture of *Microcystis aeruginosa*

Microcystis aeruginosa FACHB-905 was purchased from the Institute of Aquatic Biology, Chinese Academy of Sciences

(Wuhan, China). The algae strain was cultured in a BG11 medium in an intelligent light incubator (PGX-600B, Ningbo Saifu Experimental Instrument Co., Ltd, China) with a light–dark ratio of 12 h/12 h, a temperature of 25 °C, and a light intensity of 40 $\mu mol\ m^{-2}\ s^{-1}$. The growth of the exponential stage was maintained by the subculture. The density of algae cells was obtained from the absorbance value of algae cells at 680 nm (OD_{680}).

Characterization methods

The thermal stability of the prepared materials was tested using a thermogravimetric analyzer (TGA, NETZSCHTG 209) from room temperature to 800 °C. The phase of the synthesized photocatalyst was analyzed using an X-ray diffractometer (Rigaku D/max 2550, Japan) within the range of 10°–80°. The functional groups and chemical bonds were measured using a Fourier transform infrared spectrometer (Thermo Scientific Nicolet 6700, USA). The morphology of the material was characterized using scanning electron microscopy (SEM, SU 8010, Japan) equipped with an energy-dispersive X-ray spectroscopy (EDS) system. The EDS analysis was conducted at an accelerating voltage of 15 kV and a working distance of 10 mm. The spectra were collected for a live time of 60 s. The specific surface area and pore size of the samples were measured by N_2 adsorption–desorption isotherms at 77 K using a specific surface area analyzer (Micromeritics ASAP 2460, USA). The surface hydroxyl content of the catalyst was determined *via* Boehm titration,[19] as described in the SI.

Inactivation experimental method

The prepared material (0.2 g L^{-1}) was added to a 50 mL suspension of *Microcystis aeruginosa* with a cell density of 3×10^6 cells per mL and placed in the photocatalytic reactor. Fig. S1 shows the experimental setup. Circulating water was used to eliminate the thermal effects of xenon lamps, and slow magnetic stirring was used to simulate the natural flow of water. First, a sample was taken after 30 min of stirring in the dark. Then, the 200 W xenon lamp was turned on for photocatalysis for 7 h, and a sample was taken every 1 h. The Chl *a* concentration in the algal solution was measured using a phytoplankton fluorometer (Phyto-PAM). The changes in the extracellular organic matter content in the algal solution were analyzed using a three-dimensional fluorescence spectrometer, and the algal toxin concentration in the algal solution was determined using an ELISA algal toxin kit. The inactivation rate of *Microcystis aeruginosa* was calculated as follows:

$$\text{Removal rate}(\%) = \frac{C_0 - C_t}{C_0} \times 100\% \quad (1)$$

where C_0 and C_t are the initial concentration and residual concentration (cells per mL) of algal cells, respectively.

The intracellular organic matter and extracellular organic matter of *Microcystis aeruginosa* during the inactivation process were tested using a high-speed 3D excitation-emission matrix (EEM) spectrometer (Horiba, Aqualog, Japan). After filtration through a 0.22 μm membrane filter, the concentration of MC-LR

was analyzed by high-performance liquid chromatography (HPLC, HITACHI, Japan). The detailed methods are provided in the SI. The effects of the reaction time, pH, photocatalyst dosage, and initial algal density on the material's adsorption and photocatalytic inactivation of *Microcystis aeruginosa* were studied. The RSM was used to optimize the operating conditions (Tables S1 and S2).

In addition, the effects of HA, FA, BSA, and particulate matter in natural water on the inactivation of *Microcystis aeruginosa* by C–TiO$_2$, C–TiO$_2$–Fe$_3$O$_4$ and C–TiFe$_2$O$_4$ were investigated. The reaction mechanism in the inactivation process was analyzed using IPA, BQ, and SO as quenchers. Finally, the stability of C–TiO$_2$, C–TiO$_2$–Fe$_3$O$_4$ and C–TiFe$_2$O$_4$ in the inactivation process was evaluated by reusing the catalysts five times. After each run, C–TiO$_2$, C–TiO$_2$–Fe$_3$O$_4$, and C–TiFe$_2$O$_4$ were recovered by centrifugation and magnetic separation.

After 1, 3, 5, and 7 h of photocatalytic irradiation, the algae liquid was centrifuged (8000 rpm, 10 min) to obtain the bottom algae cells. Then, it was washed three times with a sterile PBS solution (0.1 M). Subsequently, the algae cells were resuspended in a PBS solution, and the cells were disrupted in an ice water bath using an ultrasonic cell disruptor and centrifuged again. The supernatant was used to determine the malondialdehyde (MDA) content and catalase (CAT) activity using a kit (Nanjing Jiancheng Bioengineering Institute, Nanjing, China).

Results and discussion

Material characterization

The crystalline phases of the prepared materials were characterized by X-ray diffraction (XRD, Fig. 1a). The XRD pattern of C–TiO$_2$ exhibited the characteristic peaks of SiO$_2$, which were observed at $2\theta = 20.86°$ (d_{100}), $26.64°$ (d_{011}), $50.14°$ (d_{211}), and $59.96°$ (d_{121}) (JCPDF # 74-1811), and the characteristic diffraction peaks of TiO$_2$, which were observed at $2\theta = 25.30°$ (d_{101}), $37.79°$ (d_{004}), $48.04°$ (d_{200}), $53.89°$ (d_{105}), and $62.11°$ (d_{213}) (JCPDF # 86-1157). The C–TiO$_2$–Fe$_3$O$_4$ composite maintained these SiO$_2$ and TiO$_2$ diffraction peaks while showing distinct Fe$_3$O$_4$ (magnetite) peaks (JCPDF #19-629), which were observed at $2\theta = 35.43°$ (d_{311}), $43.05°$ (d_{400}), and $56.94°$ (d_{222}). C–TiFe$_2$O$_4$ retained the characteristic diffraction peaks of TiO$_2$ and exhibited the characteristic diffraction peaks of TiFe$_2$O$_4$, which were observed at $2\theta = 35.26°$ (d_{-110}), $40.29°$ (d_{210}), $53.04°$ (d_{321}), $63.28°$ (d_{211}), and $70.08°$ (d_{433}) (JCPDF # 29-073).

Fourier transform infrared (FTIR) spectroscopy was used to characterize the surface functional groups of the synthesized materials (Fig. 1b). For all samples, the peak at 1632 cm^{-1} corresponded to the bending vibrations of the H$_2$O molecule,[20] and the peak at 3436 cm^{-1} represented the bending and stretching vibrations of the hydroxyl group (–OH).[21] According to the FTIR spectrum of TiO$_2$, the absorption peak at 600–1000 cm^{-1} corresponded to the Ti–O–Ti band.[22] Except for the absorption peak of the carbon-free functional group of TiO$_2$, the TiO$_2$ absorption peaks of other materials appeared near 710 cm^{-1}. The absorption band in the range of 875–1035 cm^{-1} was related to the C–O stretching and –OH deformation of the aliphatic carbon chain. The absorption band in the range of
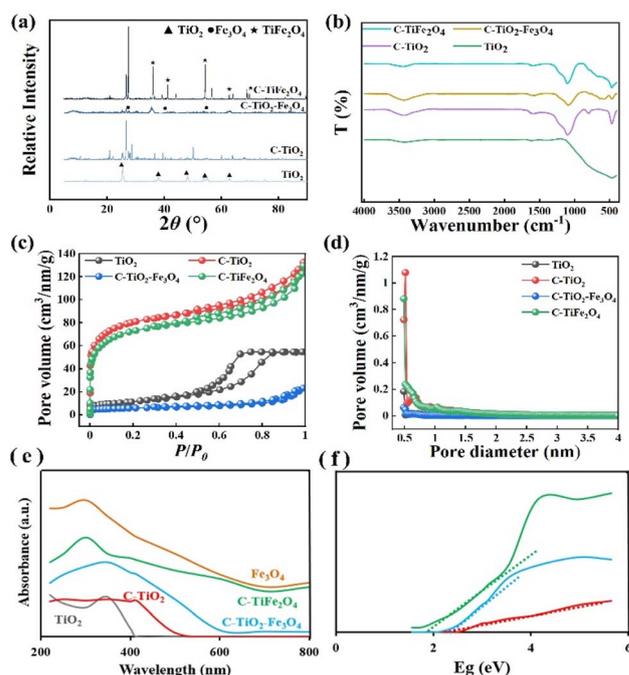

Fig. 1 (a) XRD patterns, (b) FTIR spectra, (c) BET patterns, (d) corresponding pore size distribution curves, (e) absorbance spectra, and (f) Tauc plots of TiO$_2$, C–TiO$_2$, C–TiO$_2$–Fe$_3$O$_4$, and C–TiFe$_2$O$_4$.

1400–1425 cm^{-1} was attributed to the C–C/C=C skeleton vibration. FTIR spectroscopy confirmed the successful preparation of C–TiO$_2$, C–TiO$_2$–Fe$_3$O$_4$, and C–TiFe$_2$O$_4$.

Fig. 1c and d show the nitrogen adsorption–desorption isotherms and corresponding pore size distribution curves of the synthesized materials, respectively. Table S3 shows the detailed textural parameters. The adsorption hysteresis loop appeared in the middle section of the curve of TiO$_2$, and capillary condensation occurred, which is shown as a type-IV isotherm. The adsorption capacity of C–TiO$_2$ rapidly increased at a relatively low relative pressure, and the adsorption saturated after a certain relative pressure, *i.e.*, a type-I isotherm,[23] which is caused by micropore filling in the microporous adsorbent. After loading Fe$_3$O$_4$, the specific surface area of C–TiO$_2$–Fe$_3$O$_4$ decreased from 320.96 m^2 g^{-1} for C–TiO$_2$ to 224.62 m^2 g^{-1}. Further accumulation of Fe$_3$O$_4$ in C–TiO$_2$ reduced the specific surface area of the CMT. The C–TiO$_2$–Fe$_3$O$_4$ showed a type-I isotherm, which is caused by the micropore filling phenomenon of the microporous adsorbent. For C–TiFe$_2$O$_4$, the adsorption capacity was close to the limit value due to the restriction of the micropore volume that the adsorbed gas could enter, *i.e.*, a type-I isotherm. The specific surface area of C–TiFe$_2$O$_4$ was 260.02 m^2 g^{-1}, which is between the values of C–TiO$_2$ and C–TiO$_2$–Fe$_3$O$_4$. Thus, the one-step synthesis method effectively reduced the specific surface area of the CMT.

The micromorphology of the synthesized materials was examined by SEM (Fig. S2). The CMT retained its tubular structure despite surface roughness, which suggests that the acid treatment and high-temperature calcination minimally affect the structural integrity of the corncob-derived carbon. For

C–TiO$_2$, the presence of spherical nanoparticles on the CMT surface confirmed the successful loading of TiO. In C–TiO$_2$–Fe$_3$O$_4$, smaller spherical aggregates were observed, which indicates the incorporation of Fe$_3$O$_4$. The C–TiFe$_2$O$_4$ composite exhibited distinct rod-like crystals, which verifies the formation of TiFe$_2$O$_4$ on the CMT support. The EDS results (Fig. S3) showed that there was Fe on C–TiO$_2$–Fe$_3$O$_4$ and C–TiFe$_2$O$_4$. Therefore, TiO$_2$, TiO$_2$–Fe$_3$O$_4$, and TiFe$_2$O$_4$ were successfully loaded on the CMT.

The surface hydroxyl groups serve as critical active sites in photocatalytic reactions, which significantly affect the material's efficiency.[24] The surface hydroxyl content of the CMT was 2.7692×10^{20} g^{-1} (Table S4). When the CMT was loaded with TiO$_2$, the surface hydroxyl content increased from 0.9632×10^{20} to 4.214×10^{20} g^{-1}. The surface hydroxyl content of C–TiO$_2$–Fe$_3$O$_4$ after loading Fe$_3$O$_4$ was 3.2508×10^{20} g^{-1}, which is lower than that of C–TiO$_2$, so C–TiO$_2$–Fe$_3$O$_4$ has a slightly lower photocatalytic performance than C–TiO$_2$. In addition, the surface hydroxyl content of C–TiFe$_2$O$_4$ was 4.634×10^{20} g^{-1}, which is higher than that of C–TiO$_2$ and C–TiO$_2$–Fe$_3$O$_4$. The hydroxyl content trends strongly correlate with the expected photocatalytic activities of these materials, which is consistent with their roles as active reaction sites. It is speculated that C–TiFe$_2$O$_4$ has a slightly higher photocatalytic performance than C–TiO$_2$ and C–TiO$_2$–Fe$_3$O$_4$.

A DRS device was used to determine the reflectance spectra to obtain the optical responses of the TiO$_2$, Fe$_3$O$_4$, C–TiO$_2$, C–TiO$_2$–Fe$_3$O$_4$, and C–TiFe$_2$O$_4$ (Fig. 1e). The bandgap of the samples was calculated by eqn (2):

$$E_g = hc/\lambda \tag{2}$$

where E_g is the bandgap energy (eV), h is the Planck constant, c is the light velocity (m s^{-1}), and λ is the wavelength (nm).

The DRS spectra of the nanocomposite indicated significant absorption of C–TiO$_2$, C–TiO$_2$–Fe$_3$O$_4$, and C–TiFe$_2$O$_4$ at 420 nm and 385 nm, respectively. The bandgap energies of C–TiO$_2$, C–TiO$_2$–Fe$_3$O$_4$, and C–TiFe$_2$O$_4$ were 2.02 eV, 2.37 eV, and 1.87 eV (Fig. 1f), respectively. According to these results, the bandgap energy of C–TiFe$_2$O$_4$ is lower than that of TiO$_2$ (3.52 eV) and C–TiO$_2$–Fe$_3$O$_4$ (2.37 eV), which shows a red shift in the spectra following the C–TiFe$_2$O$_4$ formation, extending the range from UV light to UV-VIS light. The reduced band gap values of the composites favor the separation of electrons and holes.[25] Moreover, the electron–hole recombination in the C–TiFe$_2$O$_4$ is prevented, causing an increase in the electron density. Therefore, the visible light absorption of C–TiFe$_2$O$_4$ is improved.

Inactivation of *Microcystis aeruginosa* by the prepared materials

To evaluate the inactivation of *Microcystis aeruginosa* by C–TiO$_2$, C–TiO$_2$–Fe$_3$O$_4$, and C–TiFe$_2$O$_4$, the Chl *a* content, Fv/Fm, and pH values of *Microcystis aeruginosa* during the inactivation process were measured (Fig. 2). Fig. S4 shows the actual picture of algae inactivation.

Chl *a*, which is the primary photosynthetic pigment in algae, plays a crucial role in light energy absorption and conversion, so
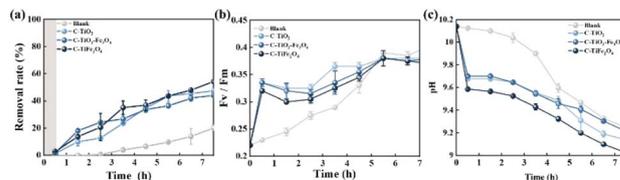

Fig. 2 Changes in the (a) Chl *a* content, (b) Fv/Fm, and (c) pH during the inactivation of *Microcystis aeruginosa* by the prepared materials.

its content variation is a reliable indicator for assessing algal cell inactivation. In the control group (without photocatalysts), the Chl *a* content first increased and subsequently gradually decreased, which suggests the adaptive stress response of algal cells to environmental changes; ultimately, 20.2% inactivation occurred after 7 h of xenon lamp irradiation and magnetic stirring. Notably, the introduction of photocatalysts significantly enhanced the inactivation efficiency: C–TiO$_2$, C–TiO$_2$–Fe$_3$O$_4$, and C–TiFe$_2$O$_4$ achieved 47.2%, 44.1%, and 54.3% inactivation rates, respectively, which demonstrates the superior performance of C–TiFe$_2$O$_4$. The photosynthetic activity (Fv/Fm) monitoring revealed complex dynamics: the control group showed a steady increase (from 0.22 to 0.41), whereas the catalyst-treated groups exhibited a rapid initial rise (*e.g.*, C–TiO$_2$ from 0.22 to 0.33 within 0.5 h), a subsequent decline (to 0.32 at 2.5 h), and an eventual recovery (to 0.38 at 7.5 h), which may indicate the photoadaptation of surviving cells. Concurrently, the system's pH gradually decreased from 10.14 to 9.24 in the control group, while more pronounced reductions were observed in the catalyst-amended systems (C–TiO$_2$: 9.14; C–TiO$_2$–Fe$_3$O$_4$: 9.21; and C–TiFe$_2$O$_4$: 9.03), suggesting that photocatalytic degradation of cellular components contributes to medium acidification.

SEM observations (Fig. S5) revealed distinct morphological differences between the control and photocatalyst-treated algal cells after 7 h of treatment. The blank control group maintained intact cellular structures with smooth surfaces and well-defined contours. In contrast, algal cells exposed to photocatalytic treatment (C–TiO$_2$, C–TiO$_2$–Fe$_3$O$_4$, and C–TiFe$_2$O$_4$) exhibited significant surface deformation, characterized by pronounced wrinkling and cell wall rupture. These morphological alterations likely result from photocatalytic oxidation-induced membrane damage and subsequent cell lysis. The observed cellular collapse correlates with the measured pH reduction, which suggests that the intracellular fluid leakage contributes to the medium acidification. Notably, C–TiFe$_2$O$_4$-treated cells displayed the most severe structural damage, which is consistent with its superior inactivation performance.

The inactivation kinetics of C–TiO$_2$, C–TiO$_2$–Fe$_3$O$_4$ and C–TiFe$_2$O$_4$ were consistent with Langmuir–Hinshelwood (L–H) models (SI), as shown in Fig. 3. With an increase in the initial algal density, the first-order kinetic reaction rate, K, gradually decreased. When the initial algal density increased from 1×10^6 to 1×10^7 cells per mL, the K value of C–TiO$_2$ decreased from 0.161 to 0.049 min^{-1}, the K value of C–TiO$_2$–Fe$_3$O$_4$ decreased from 0.084 to 0.073 min^{-1}, and the K value of C–TiFe$_2$O$_4$ decreased from 0.115 to
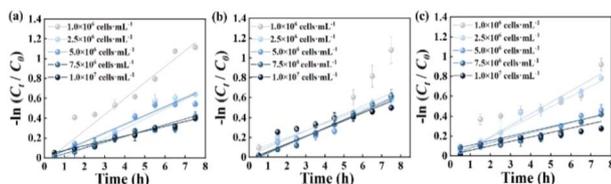
Fig. 3 L–H model fitting of (a) C–TiO$_2$, (b) C–TiO$_2$–Fe$_3$O$_4$ and (c) C–TiFe$_2$O$_4$.

Fig. 4 Changes in MC-LR during the inactivation of *Microcystis aeruginosa* by the prepared materials.

0.045 min^{-1}. The reason for this phenomenon may be that with an increase in the initial algal density, more intermediates accumulate in the photoinactivation process, which form a competitive relationship with algal cells and decrease the photoinactivation reaction rate.

Effect of the prepared materials on the release of organic matter from algae cells

During the photoinactivation of algal cells, the rupture of cellular structures releases organic matter into water, which exacerbates organic pollution. Therefore, organic matter removal and algal cell inactivation must be simultaneously addressed. A three-dimensional fluorescence analysis was conducted on algae solutions treated with C–TiO$_2$, C–TiO$_2$–Fe$_3$O$_4$, and C–TiFe$_2$O$_4$ after 1 h, 4 h, and 7 h of visible-light irradiation (Fig. S6). The analysis revealed distinct peaks: Peak A ($\lambda_{ex}/\lambda_{em}$ = 280/325 nm) corresponded to protein-like substances, Peak B ($\lambda_{ex}/\lambda_{em}$ = 255/655 nm) corresponded to fulvic acid-like compounds, and Peak C ($\lambda_{ex}/\lambda_{em}$ = 345/625 nm) corresponded to humic acid. The fluorescence intensity of these peaks decreased over time, which indicates that the photocatalysts effectively oxidize and remove the organic matter released by the algal cells. In the blank group, only a slight reduction in extracellular organic matter was observed. In contrast, the addition of C–TiO$_2$, C–TiO$_2$–Fe$_3$O$_4$, and C–TiFe$_2$O$_4$ significantly enhanced organic matter removal, which demonstrates the strong oxidative degradation capability of the photocatalytic process on extracellular organics. The observed changes in fluorescence characteristics further confirm the changes in functional groups and prove the practical efficacy of these three photocatalytic materials.

The rupture of algal cells releases cyanobacterial toxins into the surrounding water and poses persistent toxic threats to aquatic organisms. Consequently, the simultaneous degradation of algal cells and microcystins remains a critical challenge in related research. As shown in Fig. 4, the prepared materials were evaluated for the photocatalytic degradation of MC-LR in the presence of *Microcystis aeruginosa*. In the blank group, the MC-LR concentration only slightly decreased over 7 hours, which confirms negligible degradation under only visible light. In contrast, C–TiO$_2$, C–TiO$_2$–Fe$_3$O$_4$, and C–TiFe$_2$O$_4$ achieved MC-LR removal rates of 65.6%, 74.4%, and 89.1%, respectively. However, compared to previous studies on the MC-LR degradation without algal cells,[18] the presence of *Microcystis aeruginosa* reduced the efficiency of the photocatalytic composites. This inhibition may stem from the preferential interaction
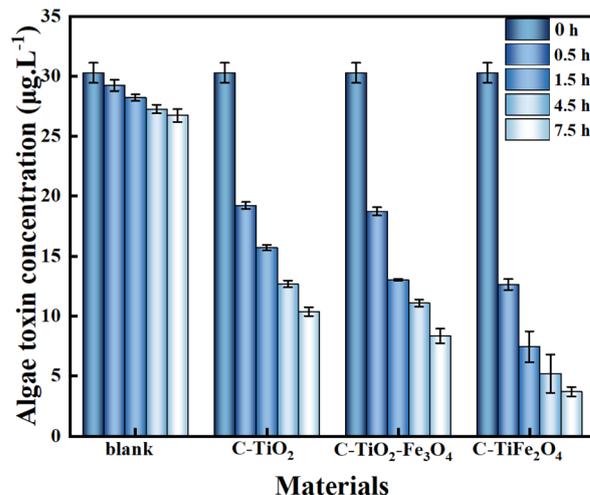
between the rough surface structure of algal cells and the active sites of the catalyst, which limits access to free MC-LR. These results demonstrate that C–TiO$_2$, C–TiO$_2$–Fe$_3$O$_4$, and C–TiFe$_2$O$_4$ effectively remove both *Microcystis aeruginosa* and the organic matter released during cell lysis.

The reaction intermediates of MC-LR were analyzed by HPLC-MS. The possible intermediates, oxidative groups, and bond energy sites were studied. After 30 min and 60 min of light irradiation, at least 8 intermediate products were identified in the total ion chromatogram (TIC), as shown in Fig. S7a and b. So, the possible degradation pathways of MC-LR in the C–TiFe$_2$O$_4$ photocatalytic procedure were proposed (Fig. S7c). The hydrolysis of the MC-LR peptide bond was rapid by C–TiFe$_2$O$_4$. First, the intermediate product m/z = 856 was produced by the loss of the D-Arg fragment (Path 1), and then, it was hydrolyzed by the peptide bond D-Leu-MeAsp-Ala-Mdha and underwent carboxyl oxidation to form the product m/z = 468. Then, the photocatalytic system further hydrolyzed the peptide bond Glu, followed by carboxyl oxidation to form the products m/z = 336 and m/z = 228. The product of m/z = 780 was hydrolyzed by peptide bonds (Path 2). Most of the oxidation products, such as m/z = 856 and 780, were not similar to the oxidation products produced by typical photocatalysis, so the degradation of this system involved alternating degradation pathways. The intermediate product fragments m/z = 414 and 267 originated from peptide bond hydrolyzation and carboxyl oxidation. The final products m/z = 336 and 228, produced by the hydrolysis of peptide bonds in MC-LR, were more difficult to remove than MC-LR. This indicates that the catalyst preferentially interacts with the complete ring structure of MC-LR, which is composed of seven amino acids connected by peptide bonds. The first 30 min of C–TiFe$_2$O$_4$ photocatalysis mainly involves hydrolysis to open the macrocycle, followed by decomposition up to 60 min, resulting in a significant increase in small molecular fragments at 90 min. Opening the ring structure of MC-LR by photocatalysis can significantly reduce its toxicity. Therefore,

the selectivity of C–TiFe$_2$O$_4$ toward the cyclic structure in the first 30 min affords the photocatalytic system good application prospects.

Effects of different parameters on the inactivation of *Microcystis aeruginosa*

Single-factor experiments were conducted to evaluate the effects of the pH, catalyst dosage, initial algal density, and reaction time on the performance of C–TiO$_2$, C–TiO$_2$–Fe$_3$O$_4$, and C–TiFe$_2$O$_4$. Among these parameters, the catalyst dosage plays a crucial role in the removal efficiency and economic feasibility. As shown in Fig. 5a, d, and g, the algal removal efficiency generally increased with increasing photocatalyst concentrations in a certain range. For example, as the C–TiFe$_2$O$_4$ dosage increased from 0.1 to 0.4 g L^{-1}, the algal inactivation rate increased from 47.2 to 75.6%, which is attributed to the enhanced contact between algae and the photocatalyst. However, further increasing the dosage to 0.5 g L^{-1} reduced the inactivation rate to 54.2%. This trend aligns with the findings of Fan *et al.*,[26] who reported that ZnFe$_2$O$_4$/Ag$_3$PO$_4$/g-C$_3$N$_4$ exhibited optimal algal inactivation at 100 mg L^{-1}, but the efficiency declined at higher dosages due to light-shielding effects that hindered the photocatalyst activation.[27] Therefore, the optimal dosage for C–TiO$_2$, C–TiO$_2$–Fe$_3$O$_4$, and C–TiFe$_2$O$_4$ was determined to be 0.4 g L^{-1}.

The photocatalytic inactivation efficiency of C–TiO$_2$, C–TiO$_2$–Fe$_3$O$_4$, and C–TiFe$_2$O$_4$ remained relatively stable across the pH range of 7.5–10.5 (Fig. 5b, e and h). Under alkaline conditions, the photoexcited holes in the catalysts reacted with hydroxide ions (OH$^-$) to generate hydroxyl radicals ($\cdot$OH), which induced oxidative damage to algal cells. Notably, at pH 11.5, C–TiO$_2$–Fe$_3$O$_4$ and C–TiFe$_2$O$_4$ exhibited significantly enhanced inactivation rates, which is primarily attributed to the severe cellular damage of the highly alkaline environment itself.
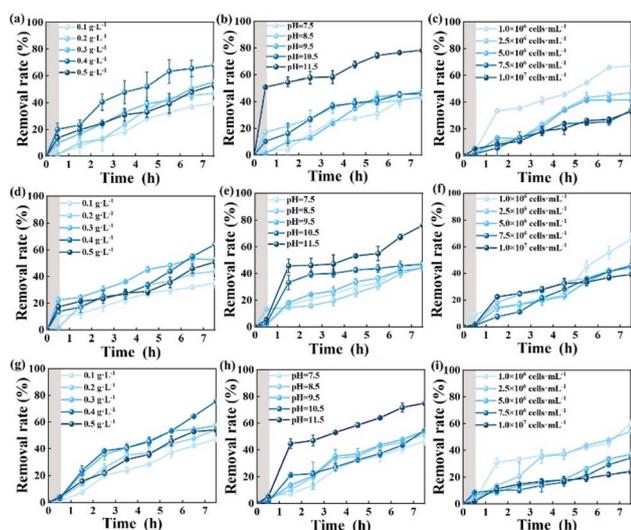
The inactivation efficiency of C–TiO$_2$, C–TiO$_2$–Fe$_3$O$_4$, and C–TiFe$_2$O$_4$ exhibited an inverse relationship with the initial algal density (Fig. 5c, f and i). This trend can be attributed to two primary factors: (1) the fixed catalyst dosage is insufficient for generating sufficient reactive species for higher cell concentrations and (2) an increased algal density reduces light penetration through the suspension. At an initial algal density of 1 × 10^6 cells per mL, rapid inactivation occurred when the catalysts provided abundant active sites relative to the algal concentration.[28] However, when the density increased to 1 × 10^7 cells per mL, the inactivation rate of C–TiFe$_2$O$_4$ significantly decreased from 54.1 to 24.2%, which demonstrates the limitation of a fixed catalyst dosage in treating high-density algal suspensions.

Among the tested materials, C–TiFe$_2$O$_4$ consistently showed superior performance, with the highest inactivation rates under all experimental conditions. The optimum conditions validated that the removal rate of C–TiFe$_2$O$_4$ could reach above 75% (Fig. S8–S11). A comparative analysis with literature values (Table S6) confirmed its advantages, including the lower required catalyst dosage and higher relative inactivation efficiency than those of other photocatalytic systems.

Inactivation effect of *Microcystis aeruginosa* in simulated natural water

To simulate natural eutrophic waters, the following representative constituents were selected for evaluation: HA, FA, BSA, and particulate matter (SiO$_2$).[29] Interestingly, at concentrations below 4 mg L^{-1}, these organic substances enhanced algal inactivation by the photocatalysts (Fig. 6). For example, with 1 mg L^{-1} HA, the removal efficiencies of C–TiO$_2$, C–TiO$_2$–Fe$_3$O$_4$, and C–TiFe$_2$O$_4$ increased from 47.2%, 44.1%, and 54.3 to 48.2%, 50.3%, and 62.1%, respectively. This enhancement occurred because these organic compounds acted as effective hole scavengers, captured photogenerated holes and facilitated electron–hole separation.[30] The resulting increase in available photogenerated electrons consequently boosted photocatalytic activity against algal cells. However, beyond 4 mg L^{-1}, these

Fig. 5 Effects of C–TiO$_2$, C–TiO$_2$–Fe$_3$O$_4$ and C–TiFe$_2$O$_4$ on the inactivation of *Microcystis aeruginosa* at different (a, d and g) catalyst dosages, (b, e and h) pH values and (c, f and i) initial algae concentrations.
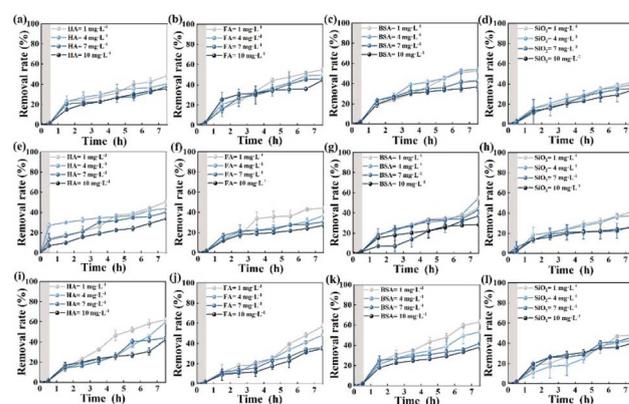
Fig. 6 Effects of (a, e and i) HA, (b, f and j) FA, (c, g and k) BSA, and (d, h and l) SiO$_2$ in natural water on the inactivation of *Microcystis aeruginosa* by C–TiO$_2$, C–TiO$_2$–Fe$_3$O$_4$, and C–TiFe$_2$O$_4$, respectively.

organics exhibited concentration-dependent inhibition. In 10 mg L^{-1} HA, the removal rates decreased by 26%, 24%, and 31.5% for C–TiO$_2$, C–TiO$_2$–Fe$_3$O$_4$, and C–TiFe$_2$O$_4$, respectively. Similarly, 10 mg L^{-1} FA caused reductions of 35.6%, 33.9%, and 42.2%, respectively. This reversal occurs through two mechanisms: (1) competitive occupation of photocatalytically active sites by organic molecules and algal cells[31] and (2) increased solution turbidity due to dissolved organics, which leads to significant light-shielding effects.[32] The transition from the promoter to the inhibitor at approximately 4 mg L^{-1} demonstrates the delicate balance between beneficial charge separation and detrimental light attenuation/competition effects in natural water remediation.

To evaluate the effects of natural water constituents, silica (SiO$_2$) was introduced as a model particulate matter to examine its impact on the photocatalytic inactivation of *Microcystis aeruginosa* (Fig. 6d, h and l). The results demonstrated a clear inverse relationship between the SiO$_2$ concentration and algal removal efficiency. As the SiO$_2$ concentration increased from 1 to 10 mg L^{-1}, the removal rates decreased by 7.9%, 15.7%, and 8.7% for C–TiO$_2$, C–TiO$_2$–Fe$_3$O$_4$, and C–TiFe$_2$O$_4$, respectively. This decrease in efficiency can be attributed to light scattering by suspended particles, which significantly diminishes light penetration and consequently reduces photon utilization by the photocatalysts.[33]

In summary, high concentrations of HA, FA, BSA, and particulate matter in natural water inhibited the photoinactivation of *Microcystis aeruginosa* by C–TiO$_2$, C–TiO$_2$–Fe$_3$O$_4$ and C–TiFe$_2$O$_4$. However, at lower concentrations of HA, FA, and BSA (<4 mg L^{-1}), the presence of hole scavengers increased the removal rate of *Microcystis aeruginosa* by the prepared materials.

Stability of the catalysts

The stability of C–TiO$_2$, C–TiO$_2$–Fe$_3$O$_4$, and C–TiFe$_2$O$_4$ was evaluated by repeated inactivation experiments. All three photocatalysts showed stable activity (Fig. 7). After 5 runs, the removal rates of C–TiO$_2$, C–TiO$_2$–Fe$_3$O$_4$, and C–TiFe$_2$O$_4$ decreased from 47.2 to 43.9%, 43.9 to 40.2%, and 54.2 to 50.4%, respectively. The XRD patterns showed that the structures of C–TiO$_2$, C–TiO$_2$–Fe$_3$O$_4$, and C–TiFe$_2$O$_4$ were similar before and after photocatalytic inactivation. Peak positions were identical, and only slight shifts in peak intensities were observed, which further demonstrates that the C–TiO$_2$, C–TiO$_2$–Fe$_3$O$_4$, and C–TiFe$_2$O$_4$ possess reusable and sustainable removal performance during multiple removal processes. The XRD peak shifts may be related to the following two reasons: after adsorption on the surface of the photocatalyst, the water molecules form hydrogen bonds with the surface hydroxyl groups, which may cause a certain degree of relaxation of the surface lattice, or the catalyst surface may form some carbon-containing intermediate products in the photocatalytic process. These intermediate products may change the structure of the catalyst surface, which may eventually lead to a slight shift in the XRD peak position. Therefore, the catalytic activity of C–TiO$_2$, C–TiO$_2$–Fe$_3$O$_4$, and C–TiFe$_2$O$_4$ did not significantly decrease after five cycles. These
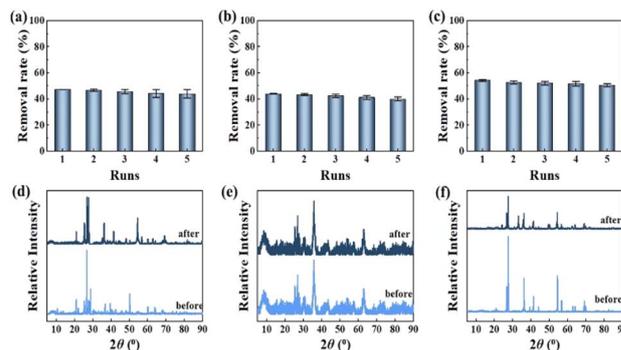
Fig. 7 Stability of recovered (a) C–TiO$_2$, (b) C–TiO$_2$–Fe$_3$O$_4$, and (c) C–TiFe$_2$O$_4$. XRD patterns of (d) C–TiO$_2$, (e) C–TiO$_2$–Fe$_3$O$_4$ and (f) C–TiFe$_2$O$_4$ before and after recycling.

results show that C–TiO$_2$, C–TiO$_2$–Fe$_3$O$_4$, and C–TiFe$_2$O$_4$ have good stability, and there is no change in their physical and chemical properties during the inactivation process, which has broad application prospects in the treatment of cyanobacterial blooms.

Active species to capture the experiment

Photocatalytic activity is predominantly governed by the formation of reactive oxygen species (ROS; ˙OH and ˙O$_2^-$) and charge carriers (h$^+$), which mediate the redox reaction. To explore the role of photoactive substances in the reaction process, the main reactive oxygen species in the C–TiO$_2$ photocatalytic degradation of *Microcystis aeruginosa* were determined by active species capture experiments. IPA (0.01 mol L^{-1}), SO (0.01 mol L^{-1}), and BQ (0.01 mol L^{-1}) were used as quenchers for ˙OH, h$^+$, and O$_2^-$, respectively.

The main ROS species of C–TiO$_2$, C–TiO$_2$–Fe$_3$O$_4$, and C–TiFe$_2$O$_4$ in the photocatalytic inactivation of *Microcystis aeruginosa* were determined by active species quenching experiments (Fig. 8). When BQ was added, the removal rates of C–TiO$_2$, C–TiO$_2$–Fe$_3$O$_4$, and C–TiFe$_2$O$_4$ decreased from 47.2 to 23.0%, from 43.9 to 21.5%, and from 54.2 to 22.8%, respectively. When IPA was added, the removal rate slightly decreased, whereas the removal rate remained basically unchanged when SO was added. The effect of active species on the reaction was further investigated by ESR experiments. The 1 : 1 : 1 : 1 ratio DMPO–˙O$_2$-adduct signal peaks are shown in Fig. S12, indicating the presence of a large amount of ·O$_2$- in the reaction system. The signal peaks of ˙OH with an intensity ratio of 1 : 2 : 2 : 1 were also detected during the experiment. The results of ESR
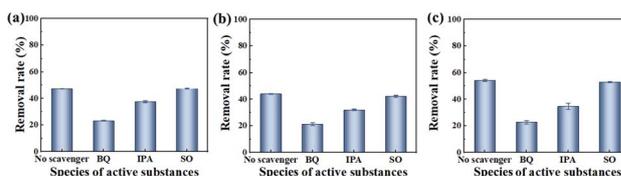

Fig. 8 Active species quenching experiments: (a) C–TiO$_2$; (b) C–TiO$_2$–Fe$_3$O$_4$; and (c) C–TiFe$_2$O$_4$.

corroborated the results of the free radical quenching experiment. The results showed that $^{\bullet}OH$ and $^{\bullet}O_2^-$ may be the main active substances in the photoinactivation of *Microcystis aeruginosa* by C–TiO$_2$, C–TiO$_2$–Fe$_3$O$_4$, and C–TiFe$_2$O$_4$.

Oxidative stress level of algal cells

With prolonged light irradiation, *Microcystis aeruginosa* experiences oxidative damage from reactive oxygen species (ROS), which destroys algal cells during the photocatalytic process. Malondialdehyde (MDA), which is a harmful byproduct of lipid peroxidation, is generated in large quantities when ROS attack the cell membrane. The MDA content serves as an indicator of the cellular lipid peroxidation severity and algal stress levels.[34] Once the MDA accumulation reaches a critical threshold, the cell membrane system becomes compromised, disrupting the essential metabolic activities that rely on membrane integrity. To counteract this damage, the antioxidant system is activated, scavenging excess intracellular ROS and preventing ROS-induced apoptosis. This defense mechanism operates through both enzymatic (*e.g.*, catalase, CAT) and nonenzymatic antioxidants. CAT, which is a key antioxidant enzyme, catalyzes the decomposition of hydrogen peroxide (H_2O_2) into water and oxygen. However, if the photocatalysis causes irreversible harm to algal cells, the antioxidant enzyme system is impaired and fails to function properly.

The samples of *Microcystis aeruginosa* treated *via* C–TiFe$_2$O$_4$ photocatalysis for 1, 3, 5, and 7 hours were analyzed to determine the MDA and CAT levels (Fig. 9). The results showed a continuous increase in the MDA content, which reflects the progressive accumulation of lipid peroxidation products during photocatalysis. In the control group, the CAT activity transiently increased before stabilizing, which indicates that endogenous CAT levels are sufficient to neutralize H_2O_2 generated under visible-light exposure. In contrast, the experimental group exhibited a rapid initial increase in CAT activity, which peaked at 5 hours before declining. This decline suggests that beyond 5 hours, the ROS scavenging demand exceeds the CAT production capacity, likely because the oxidative stress impairs the antioxidant enzyme activity.[35] The decrease in CAT levels implies that the antioxidant system can no longer fully counteract persistent oxidative damage, so peroxidation products accumulate. Consequently, the residual ROS overwhelm cellular defenses, disrupt physiological functions, and ultimately cause algal cell death.
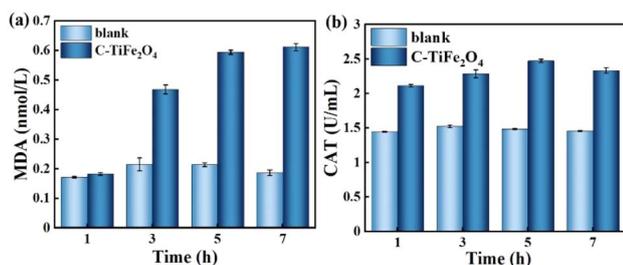

Fig. 9 Changes in the (a) MDA content and (b) CAT activity during photocatalytic inactivation.

Mechanism of algae cell destruction

Shading typically occurs when catalyst particles aggregate on algal cells, reducing the optical cross-section of their photochemical reaction centers and consequently inhibiting photosynthesis.[36] Previous studies have demonstrated this phenomenon under different conditions. For example, Schwab *et al.*[37] observed that carbon nanotubes hindered algal growth due to their shading effect, whereas Yan *et al.*[38] reported that graphene oxide (GO) extensively coated algal cell surfaces through hydrogen and covalent bonding, which exacerbated light blockage. Our findings align with these observations, which confirm that the shading effect of C–TiFe$_2$O$_4$ significantly diminishes the light absorption by algal cells and ultimately disrupts their photosynthetic activity.

C–TiO$_2$, C–TiO$_2$–Fe$_3$O$_4$, and C–TiFe$_2$O$_4$ have high specific surface areas and porous structures, which enable efficient adsorption of algal cells. These photocatalytic materials interact with algal cell walls or membranes and accumulate on their surfaces, which is called the adsorption effect.[39] Under coagulation effects, the materials penetrate cell walls and membranes *via* endocytosis, transport carrier proteins, or ion channels, which compromise structural integrity and disrupt the membrane's selective permeability. This damage accelerates the algal inactivation.[40] Supporting this mechanism, Sathe *et al.*[41] demonstrated that *Dunaliella salina* cells adsorbed onto ZnO nanorod coatings were inactivated under visible light. The high local concentration of ROS generated by ZnO oxidizes algal fatty acid chains and induces lipid deformation, membrane rupture, and subsequent DNA damage. Furthermore, the material aggregation on cell surfaces increases the algal cell density and makes them sink into deeper, light-deprived zones. This condition is detrimental to growth.[42]

The photocatalysts primarily inhibit algal growth and induce cell inactivation through oxidative stress mediated by ROS such as $^{\bullet}OH$, h^+, and $^{\bullet}O_2^-$, which are generated during photocatalytic reactions.[43] Under visible-light irradiation, C–TiO$_2$, C–TiO$_2$–Fe$_3$O$_4$, and C–TiFe$_2$O$_4$ are activated and produce electron–hole pairs. In these carbon-modified titanium-based materials, photogenerated electrons (e^-) migrate from the valence band (VB) to the conduction band (CB) and leave behind holes (h^+). These accumulated h^+ react with the adsorbed H_2O molecules to form highly oxidative $^{\bullet}OH$ radicals. The sustained attack by $^{\bullet}OH$ radicals causes a progressive increase in malondialdehyde (MDA) levels, which indicates severe lipid peroxidation. This oxidative damage paralyzes the cell membrane system, disrupts membrane-dependent metabolic activities and causes the structural denaturation of membrane proteins. Because photocatalysis inflicts irreversible damage, the algal antioxidant enzyme system is compromised, so excess ROS is unquenched. The resulting oxidative stress ultimately causes cell death, which is accompanied by the release and subsequent photolysis of intracellular toxins, extracellular organic matter, and metabolites.[44]

The photocatalytic inactivation of algal cells occurs through a synergistic mechanism with three primary effects: (1) the shading effect of C–TiO$_2$–Fe$_3$O$_4$ and C–TiFe$_2$O$_4$ significantly

reduces the light availability and impairs the normal photosynthetic activity; (2) the coagulation effect from direct photocatalyst-algae contact physically damages the cell walls and membranes; and (3) photocatalytic chemical oxidation generates abundant $\cdot OH$ radicals that persistently oxidize cellular components, which triggers the lipid peroxidation and overwhelms the antioxidant defense system. The combined action of these effects (shading, coagulation, and oxidative damage) ultimately completely inactivates the algal cells.

Conclusions

This study reports the successful development of two carbon microtube-supported photocatalysts (C–TiO$_2$–Fe$_3$O$_4$ and C–TiFe$_2$O$_4$), all of which demonstrate effective algae removal performance. Among them, the C–TiFe$_2$O$_4$ composite exhibits the highest efficiency for inactivating *Microcystis aeruginosa*, achieving a 77.9% algal cell removal rate under optimal conditions (7 h reaction time, 0.39 g L^{-1} catalyst dosage, and an initial algal density of 1×10^6 cells per mL). This photocatalyst also removes 89.1% of MC-LR, confirming its dual functionality in both algal inactivation and toxin degradation. The algal inactivation mechanism involves shading, coagulation, and oxidation effects. These findings indicate that the C–TiFe$_2$O$_4$ photocatalyst holds significant potential for practical application in controlling harmful algal blooms and mitigating associated organic water pollution.

Author contributions

Wenli Qin: software, supervision and writing – review and editing; Xinyi Zhang: methodology, software, and writing – original draft preparation; Gaofeng Chen: data curation and methodology; Zhaoting Ji: data curation and methodology; and Zengling Ma: supervision and writing – review and editing.

Conflicts of interest

There are no conflicts to declare.

Data availability

The datasets used and analyzed during the current study are available from the corresponding author on reasonable request.

Supplementary information (SI): supporting figures and tables. See DOI: https://doi.org/10.1039/d6ra00677a.

Acknowledgements

References

1 I. Y. Massey, M. A. Osman and F. Yang, *Toxin Rev.*, 2022, **41**, 326–346.
2 X. Li, H. Zhai, J. Luo, *et al.*, *Water Res.*, 2024, **260**, 121894.
3 M. Wang, H. Zhang, C. Du, W. Zhang, J. Shen, S. Yang and L. Yang, *Environ. Pollut.*, 2021, **271**, 116294.
4 Y. Zhang, J. K. Whalen, C. Cai, *et al.*, *Water Res.*, 2023, **233**, 119807.
5 Y. Peng, X. Yang, H. Huang, *et al.*, *Chemosphere*, 2023, **323**, 138279.
6 B. Balaji-Prasath, Y. Wang, Y. P. Su, *et al.*, *Environ. Chem. Lett.*, 2022, **20**, 3133–3152.
7 M. Ke, L. Feng, S. Huang, *et al.*, *J. Agric. Food Chem.*, 2022, **70**, 10134–10143.
8 Y. Mao, H. Fan, H. Yao, *et al.*, *Sci. Total Environ.*, 2024, **917**, 170357.
9 Q. Zhai, L. Song, X. Ji, *et al.*, *Environ. Sci. Pollut. Res.*, 2022, **29**, 40449–40461.
10 L. Hu, R. Wang, M. Wang, *et al.*, *Environ. Sci. Pollut. Res.*, 2022, **29**, 47902–47914.
11 S. Lee, L. M. Lozano-Sánchez, *et al.*, *J. Hazard. Mater.*, 2013, **263**, 20–27.
12 X. Wei, H. Zhu, J. Xiong, *et al.*, *New J. Chem.*, 2021, **45**, 17483–17492.
13 S. Sun, Q. Tang, T. Yu, *et al.*, *Environ. Res.*, 2022, **215**, 114216.
14 C. Yuan, C. H. Hung, H. W. Li, *et al.*, *Chemosphere*, 2016, **155**, 471.
15 T. M. Triantis, T. Fotiou, T. Kaloudis, *et al.*, *J. Hazard. Mater.*, 2012, **211**(212), 196–202.
16 X. Zheng, X. Y. Zhang, Q. L. Hu, *et al.*, *Curr. Nanosci.*, 2021, **17**(3), 484–493.
17 X. D. Yu, X. C. Lin, W. Feng, *et al.*, *Catal. Lett.*, 2019, **149**, 552–560.
18 X. Zhang, T. Xia, Y. Meng, *et al.*, *Water*, 2025, **17**(1342), 1–24.
19 G. W. Sears, *Anal. Chem.*, 1956, **28**(12), 1981–1983.
20 J. N. Rahimi, A. Abdolahnejad and H. Farrokhzadeh, *J. Environ. Chem. Eng.*, 2019, **7**(4), 103253.
21 H. Zangene, M. Farhadian and A. Zinatizadeh, *J. Environ. Chem. Eng.*, 2020, **8**, 103639.
22 E. A. Rahimi, *J. Taiwan Inst. Chem. Eng.*, 2019, **101**, 64–79.
23 X. Y. Pan, K. K. Hou, Y. F. Zheng, *et al.*, *Chemical reaction engineering and process*, 2022, **38**(01), 23–31+40.
24 T. Xu, M. H. Jiang, X. H. Mao, *et al.*, *Appl. Catal. B: Environ.*, 2025, **372**, 125321.
25 X. Jia, J. Zhang, Q. Huang, *et al.*, *Environ. Res.*, 2024, **241**, 117639.
26 G. D. Fan, X. Lin, Y. F. You, *et al.*, *J. Hazard. Mater.*, 2022, **421**, 126703.
27 T. M. Triantis, T. Fotiou, T. Kaloudis, *et al.*, *J. Hazard. Mater.*, 2012, **211**(212), 196–202.
28 L. A. Lawton, P. K. Robertson, B. J. Cornish, *et al.*, *J. Catal.*, 2003, **213**(1), 109–113.
29 Y. F. Guo, S. S. Wu, X. D. Hu, *et al.*, *Environ. Eng.*, 2018, **36**(06), 35–41.

30 D. Xiao, *Synthesis of Modified g-C₃N₄ and Its photocatalytic reduction performance for Cr(VI)*, Huazhong Agricultural University, 2016.

31 M. Pelaez, P. Falaras, V. Likodimos, *et al.*, *J. Mol. Catal. A: Chem.*, 2016, **425**, 183–189.

32 J. Tian, C. Wu, H. Yu, *et al.*, *Water Res.*, 2018, **132**, 190–199.

33 D. Zhang, S. Yan and W. Song, *Environ. Sci. Technol.*, 2014, **48**, 12645–12653.

34 Y. Jin, H. Y. Pei, W. R. Hu, *et al.*, *Sci. Total Environ.*, 2017, **583**, 496–504.

35 W. Cui, L. Cao, J. Liu, *et al.*, *Sci. Total Environ.*, 2020, **718**, 137234.

36 J. Zhao, X. Cao, X. Liu, *et al.*, *Nanotoxicology*, 2016, **10**(9), 1297–1305.

37 F. Schwab, T. Bucheli, L. Lukhele, *et al.*, *Environ. Sci. Technol.*, 2011, **45**(14), 6136–6144.

38 Z. Yan, X. Yang, I. Lynch, *et al.*, *J. Hazard. Mater.*, 2022, **425**, 127898.

39 M. Sendra, M. Yeste, J. Gatica, *et al.*, *Sci. Total Environ.*, 2017, **592**, 403–411.

40 S. Rana and A. Kumar, *Algal Research-Biomass Biofuels and Bioproducts*, 2022, **6**, 102641.

41 P. Sathe, M. T. Z. Myint, S. Dobretsov, *et al.*, *Sep. Purif. Technol.*, 2016, **162**, 61–67.

42 G. Fan, M. Bao, X. Zheng, *et al.*, *J. Hazard. Mater.*, 2019, **367**, 529–538.

43 X. He, P. Wu, S. Wang, *et al.*, *J. Cleaner Prod.*, 2021, **289**, 125755.

44 S. Sun, Q. Tang, L. Zhou, *et al.*, *Environ. Sci. Pollut. Res.*, 2022, **29**, 29993–30003.